PRIVATE IMAGE RECONSTRUCTION FROM SYSTEM SIDE CHANNELS USING GENERATIVE MODELS

Anonymous authors
Paper under double-blind review

ABSTRACT

System side channels denote effects imposed on the underlying system and hardware when running a program, such as its accessed CPU cache lines. Side channel analysis (SCA) allows attackers to infer program secrets based on observed side channel signals. Given the ever-growing adoption of machine learning as a service (MLaaS), image analysis software on cloud platforms has been exploited by reconstructing private user images from system side channels. Nevertheless, to date, SCA is still highly challenging, requiring technical knowledge of victim software's internal operations. For existing SCA attacks, comprehending such internal operations requires heavyweight program analysis or manual efforts.

This research proposes an attack framework to reconstruct private user images processed by media software via system side channels. The framework forms an effective workflow by incorporating convolutional networks, variational autoencoders, and generative adversarial networks. Our evaluation of two popular side channels shows that the reconstructed images consistently match user inputs, making privacy leakage attacks more practical. We also show surprising results that even one-bit data read/write pattern side channels, which are deemed minimally informative, can be used to reconstruct quality images using our framework.

1 INTRODUCTION

Side channel analysis (SCA) recovers program secrets based on the victim program's nonfunctional characteristics (e.g., its execution time) that depend on the values of program secrets. SCA constitutes a major threat in today's system and hardware security landscape. System side channels, such as CPU cache accesses and operating system (OS) page table accesses made by the victim software, are widely used to recover program secrets under various real-world scenarios (Gullasch et al., 2011; Aciicmez & Koc, 2006; Wu et al., 2012; Hähnel et al., 2017; Xu et al., 2015; Yarom et al., 2017).

To conduct SCA, attackers first conduct an online phase to log a trace of side channel signals made by the victim software (e.g., its accessed CPU cache lines). Then, attackers launch an offline phase to analyze the logged trace and infer secrets (e.g., private inputs). Enabled by advances in system research, the online phase can be performed smoothly (Xu et al., 2015). Nevertheless, the offline phase is challenging, requiring comprehension of victim software's input-relevant operations and how such operations influence side channels. The influence is program-specific and obscure (see an example in Fig. 1). Even worse, side channel signals made by real-world software are usually highly noisy. For instance, executing `libjpeg` (libjpeg, 2020) to decompress an unknown JPEG image produces over 700K side channel signals, where only a small portion depends on the image content. Identifying such input-dependent signals from over 700K records is extremely difficult.

Launching SCA to recover images processed by media software constitutes a common threat in the era of cloud computing (Xu et al., 2015; Hähnel et al., 2017), especially when machine learning as a service (MLaaS) is substantially offered (e.g., for face recognition). When envisioning the high risk of violating user privacy, there is a demanding need to understand the adversarial capability of reconstructing private images with SCA. To date, the offline inference phase of existing SCA attacks requires lots of manual efforts with heuristics (Xu et al., 2015; Hähnel et al., 2017). While some preliminary studies explore to use AI models to infer secrets (Hospodar et al., 2011; Kim et al., 2019; Cagli et al., 2017; Hettwer et al., 2018), their approaches are primarily driven by *classification*, i.e.,

predicting whether a particular bit of crypto key is 0 or 1. In contrast, reconstructing user private images requires to synthesize and enhance images from a more holistic perspective.

Recent advances in generative models, such as generative adversarial network (GAN) and variational autoencoder (VAE), have enabled a major thrust in image reconstruction, given subtle signals in even cross-modal settings, e.g., voice-to-face or text-to-image (Radford et al., 2016; Reed et al., 2016; Wen et al., 2019; Hong et al., 2018b). Inspired by this breakthrough, we propose an SCA framework using generative models. Given a trace of side channel signals made by image analysis software (e.g., `libjpeg`) when processing a user input, we reconstruct an image visually similar to the input. Each logged side channel trace, containing around a million records, is first encoded into a matrix and pre-processed by a convolutional neural network (CNN) for feature extraction. Then, a VAE network with a learned prior (referred to as VAE-LP) is employed to reconstruct an image with a holistic visual appearance. We further supplement VAE-LP with a GAN model to enhance the recovered image with vivid details. The GAN generator yields the final output.

Our attack exploits media libraries, `libjpeg` (libjpeg, 2020) and `uPNG` (Middleditch, 2010), using two popular side channels, CPU cache line accesses and OS page table accesses. Our attack is independent of the underlying computing infrastructure (i.e., OS, hardware, image library implementation). We require enough side channel logs for training, which is consistently assumed by previous works (Heuser & Zohner, 2012; Maghrebi et al., 2016). While existing attacks particularly target `libjpeg` and leverage domain knowledge, system hacking, and manual efforts to infer pixel values (Xu et al., 2015; Hähnel et al., 2017), we show that images with many details can be reconstructed in an end-to-end manner. We also show surprising results that enabled by our framework, side channel traces composing *one-bit data read/write* patterns, which prima facie seems minimally informative, suffice recovering images. We conduct qualitative and quantitative evaluations on specific and general datasets representing daily images that can violate privacy if leaked. The recovered images manifest consistent visual appearances with private inputs. The recovered images also exhibit high discriminability: each recovered image (e.g., a face) can be matched to its reference input among many candidates with high accuracy. In summary, we make the following contributions:

- At the conceptual level, we present the first generative model-based SCA. Our novel approach learns how program inputs influence system side channels from historical side channel logs to reconstruct user private images automatically. We, for the first time, demonstrate surprisingly effective attacks toward even low-resolution side channels like one-bit data read/write access patterns.
- At the technical level, we design an effective framework by incorporating various design principles to facilitate image reconstruction from side channels. Our framework pipelines 2D CNN, VAE-LP, and GAN models to systematically enhance the quality of generated images.
- At the empirical level, our evaluations show that the proposed framework can generate images with vivid details and are closely similar to reference inputs. The reconstructed images show high discriminability, making privacy leakage attacks more practical.

This is the first paper to conduct SCA with generative models, revealing new SCA opportunities and unknown threats. Our code is at `https://github.com/genSCA/ICLR2021`.

2 BACKGROUND

To formulate SCA, let the attacked program be P and its input domain be I. For a deterministic and terminating program P, the program execution can be modeled as a mapping $P : I \rightarrow E$ where E represents program runtime behavior (e.g., memory access). As a common assumption (Hähnel et al., 2017), program inputs are *private* and *profitable* for attackers. Since different inputs $i, i' \in I$ can likely induce different $e, e' \in E$, using input-dependent $e \in E$ enables to infer i.

Modern computer architectures have primarily zeroed the possibility for adversaries to log $e \in E$. Nevertheless, an attacker's view on P can be modeled as a function $view : E \rightarrow O$ that maps E to *side channel* observations O. Hence, the composition $(view \circ P) : I \rightarrow O$ maps inputs to side channel signals that can be logged by attackers. The $view$ indicates the attacker's capability, and for typical system security scenarios, the $view$ is formulated as $view : E^{mem} \rightarrow O_{cache} \cup O_{page}$, where E^{mem} denotes a trace of accessed memory locations when executing P with i, and O_{cache} and O_{page} represent CPU cache and OS page table side channels, respectively. Despite being unable to monitor E^{mem}, attackers can log accessed cache lines O_{cache} or page table entries O_{page} derived from E^{mem}. Attackers then infer E^{mem} and recover i. We now concretize the procedure by introducing how SCA is used to exploit cloud platforms in a two-step approach as follows:

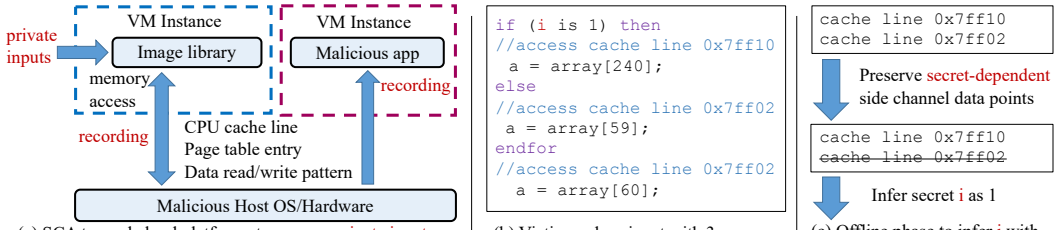

(a) SCA toward cloud platforms to recover private inputs – online side channel trace recording is straightforward.

(b) Victim code snippet with 3 memory accesses of different locations.

(c) Offline phase to infer i with the logged side channel trace.

Figure 1: Performing SCA to exploit cloud computing platforms.

Online Phase to Record O. Considering a cloud environment in Fig. 1(a), where two users, one normal and one malicious, deploy two virtual machine (VM) instances on the host. Private images $i \in I$ uploaded by users are processed by media library P within the left VM. Modern computer design, e.g., Intel SGX (Intel, 2014), guarantees that $i \in I$ and the execution of P cannot be viewed from outside the VM. However, when processing i, P usually imposes a large volume of CPU cache and page table accesses, which, as shown in Fig. 1(a), can be recorded by the co-located malicious VM or the malicious host OS in a fully automated manner (Han et al., 2017; Chiang et al., 2015; Liu et al., 2015a; Xu et al., 2015; Hähnel et al., 2017).

Offline Phase to Infer i. Once side channel traces $o \in O$ are collected, an offline phase is conducted to infer $(view \circ P)^{-1} : O \rightarrow I$ and recover i. Fig. 1(b) presents a sample code, where depending on values of input i, different memory locations (and cache lines) will be visited. Fig. 1(c) shows the corresponding trace of logged cache side channel records. To infer i, attackers eliminate the second record (since it is input-independent), and infer i as 1 according to the first record.

Attackers anticipate to 1) pinpointing a subset of records $o^* \subseteq o$ that depend on i, and to 2) recovering the mapping from o^* to i. However, real-world side channel traces (e.g., generated by `uPNG`) could contain over one million records, where only a tiny portion o^* is *input-dependent*. Even worse, constructing the mapping between i and o^* requires a deep understanding of program control flows (e.g., how `i` affects program execution and induces cache accesses in Fig. 1(b)). To date, these tasks require either manual effort (Xu et al., 2015; Hähnel et al., 2017) or formal analysis (Doychev et al., 2013; Wang et al., 2017), which are program-specific and error-prone with low scalability.

Existing research tackles the offline phase challenge by proposing *profiling-based SCA* (Maghrebi et al., 2016; Hettwer et al., 2018; Kim et al., 2019), where models are trained to approximate $(view \circ P)^{-1} : O \rightarrow I$. However, existing work focuses on predicting particular bits of crypto keys from succinct side channel traces, e.g., a few hundred records (Hettwer et al., 2020). In contrast, this is the first work shows that by incorporating generative models, SCA can be conducted to exploit real-world media libraries and holistically reconstruct high-quality and discriminable images.

3 The Proposed Framework

A common assumption shared by SCA (Heuser & Zohner, 2012; Hähnel et al., 2017; Xu et al., 2015) is that the attackers can profile the victim software locally or remotely with training inputs and collect corresponding side channel traces. We train a model to learn how different inputs can influence side channel traces. Then, given a side channel trace logged when processing an unknown image, our framework reconstructs an image that is visually similar to the unknown input.

Our framework has two pipelined modules (see Fig. 2). Given a side channel trace T_i corresponding to processing an image i, we first encode T_i into a matrix. The encoded matrix will be fed to the VAE-LP module to generate image $\hat{i}_{trace}$, and we further use GAN to denoise $\hat{i}_{trace}$ and yield the final output $\hat{i}_{GAN}$. We now elaborate on each module. More details are given in Appendix B.

3.1 Side Channel Trace Encoding

Real-world software is highly complex, and processing one image could generate a huge amount of records, where only a few records are *secret-dependent*. Processing overlong traces for previous attacks is very difficult and requires considerable domain-specific knowledge, expertise, and even manual efforts to locate and remove irrelevant records (Xu et al., 2015; Hähnel et al., 2017).

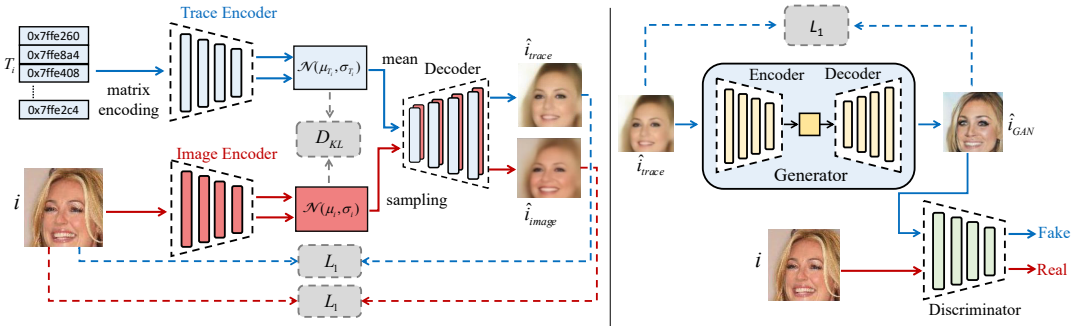

(a) VAE-LP. The training phase takes side channel traces (T_i) and reference images (i) as inputs. The predication phase only retains the upper dataflow marked in blue.

(b) GAN. This module accepts an output of the VAE-LP module and generates the final output of our framework.

Figure 2: The proposed generative framework for recovering private images from side channel traces.

Despite the general difficulty of processing overlong traces (each trace contains about 700K to 1.3M data points in our evaluation), we note that adjacent records on a side channel trace are often derived from the same or related modules (e.g., functions) of the victim software. Hence, we "fold" each side channel trace into a $N \times N \times K$ matrix to approximate spatial locality which can be further exploited by CNNs. A trace is first divided into K segments, where N adjacent points in a segment are put into one row, in total N rows. We do zero padding. CNNs are deployed in the trace encoder of VAE-LP to process the encoded matrices.

3.2 The VAE-LP Module

VAE-LP extends standard VAE by replacing its fixed Gaussian prior with a *learned prior* (Denton & Fergus, 2018), which represents the latent distribution of side channel traces. VAE-LP is trained using both real-life images and their corresponding side channel traces. By incorporating the side channel trace encoder, we can extract latent representations from the logged side channel signals. Simultaneously, by integrating corresponding reference images during training, we provide a guideline to help the image decoder to generate quality images. As shown in Fig. 2(a), the trace encoder Enc_{trace} (marked in blue) employs 2D CNNs and can extract features from side channel traces T_i in the encoded matrices. The output of Enc_{trace} constitutes the learned prior distribution of latent variable, namely $p(z_{T_i})$, rather than a fixed Gaussian distribution that VAE usually is. The decoder Dec takes the mean of $p(z_{T_i})$ as its input and outputs the image generated from side channel traces. The training phase also employs the image encoder Enc_{image} (marked in red), which accepts reference images i and outputs $q(z_i|i)$.

We train the VAE-LP network by performing forward propagation separately for two different data resources. We then use two generated images to compute reconstruction loss and perform one iteration of backward propagation. Let $\hat{i}_{trace}$ and Dec_{trace} be the generated image and Dec by conducting forward propagation with only T_i. Similarly, let $\hat{i}_{image}$ and Dec_{image} be the generated image and Dec by conducting forward propagation with only i. Parameters of Dec_{trace} and Dec_{image} are shared in the training phase, and the loss of the VAE-LP module is defined as follows:

$$Loss_{VAE-LP} = L_1(i, \hat{i}_{image}) + L_1(i, \hat{i}_{trace}) + \beta D_{KL}(q(z_i|i)||p(z_{T_i}))$$

where three terms, namely, i) a reconstruction loss $L_1(i, \hat{i}_{image})$ derived from the reference input, ii) a reconstruction loss $L_1(i, \hat{i}_{trace})$ derived from the side channel trace, and iii) a KL-divergence that forces $q(z_i|i)$ to be close to $p(z_{T_i})$ are subsumed. During the generation phase, we remove Enc_{image} and Dec_{trace}. Enc_{trace} and Dec_{image} are retained to yield $\hat{i}_{trace}$ given a logged T_i. The generative process is given by:

$$z_{T_i} \sim p(z_{T_i}) \quad \hat{i}_{trace} \sim p(i|z_{T_i})$$

3.3 The GAN Module

VAE-LP module is seen to recover $\hat{i}_{trace}$ with relatively coarse-grained information (see Sec. 5.1). As will be elaborated in Sec. 4, different private inputs can manifest *identical* side channel signals. Hence, some details are inevitably missing during input reconstruction. To tackle this inherent

Table 1: Side channels derived from a memory access made by victim software using address $addr$.

Side Channel Name	Side Channel Record Calculation
CPU Cache Line Index	$addr \gg L$ where L, denoting cache line size, is 6 on modern x86 architectures.
OS Page Table Index	$addr \,\&\, (\sim M)$ where M, denoting `PAGE_MASK`, is 4095 on modern x86 architectures.
Data Read/Write Pattern	one bit (0/1) denoting whether this memory access is a read or write operation.

limitations, we further deploy a GAN module (see Fig. 2(b)) which takes the output of the VAE-LP module, $\hat{i}_{trace}$, and generates the final output $\hat{i}_{GAN}$. To smoothly refine $\hat{i}_{trace}$, we employ an autoencoder as the generator G of GAN. The loss of the extended GAN model is defined as follows:

$$Loss_{GAN} = \gamma L_1(G(\hat{i}_{trace}), \hat{i}_{trace}) + \mathbb{E}_{i \sim p(i)}[\log D(i)] + \mathbb{E}_{\hat{i}_{trace} \sim p(\hat{i}_{trace})}[\log(1 - D(G(\hat{i}_{trace})))]$$

Compared with standard GAN, we extend the loss function with L_1 loss of $\hat{i}_{trace}$ and $G(\hat{i}_{trace})$ with a weight of γ to force G to retain the holistic visual appearance delivered by $\hat{i}_{trace}$.

4 Attack Setup

As introduced in Sec. 2, popular system side channels are primarily derived from program memory accesses. Let $addr$ be the address of a memory location accessed by the victim software, Table 1 reports three utilized side channels and how they are derived from memory accesses. Cache line and page table side channels are commonly used for exploitation (Hähnel et al., 2017; Yarom & Falkner, 2014). Furthermore, enabled by our framework, a very low-resolution side channel of data read/write access patterns can, for the first time, be used to reconstruct high-quality images. Fig. 1 holistically depicts how attackers can monitor cache and page table side channels. Data read/write patterns can be similarly recorded by monitoring how caches or page tables are visited.

Table 1 shows that different $addr$ can be mapped to the same side channel record. Similarly, different inputs can induce identical memory address $addr$. For instance, in Fig. 1(b) `array[59]` and `array[60]` will always be executed as long as $i \neq 1$. Two layers of many-to-one mapping amplify the uncertainties of synthesizing discriminable images of high quality. It is easy to see that we are **not** simply mapping a trace back to an image.

Attack Target. We attack two media libraries, `libjpeg` and `uPNG`, to reconstruct private user images of JPEG and PNG formats. Previous image reconstruction SCA (Xu et al., 2015; Hähnel et al., 2017) only exploit `libjpeg`. PNG and JPEG denote very popular image compression standards, and given an image in JPEG/PNG format, `libjpeg` and `uPNG` can reverse the compression to generate a bitmap image as the basis of many image analysis tools, e.g., the Python `Pillow` library (Clark, 2020). The decompression process introduces many input-dependent memory accesses which, from the attacker's perspective, can be reflected on side channels according to Table 1.

We share *common assumptions* with existing profiling-based SCA (Hospodar et al., 2011; Heuser & Zohner, 2012) that side channel traces have been well prepared for use. For our experiments, we use `Pin` (Luk et al., 2005), a runtime monitoring tool, to intercept memory accesses of victim software. A logged memory access trace will be converted into three side channel traces according to Table 1, denoting the attacker's view on i. Each side channel trace generated by `libjpeg` or `uPNG` contains 700K to 1.3M records. See Appendix A for attack setup details.

5 Evaluation

We present the first systematic approach to reconstructing images from side channels. There is no previous research for empirical comparison. Two closely related works provide no tools for use (Xu et al., 2015; Hähnel et al., 2017). As disclosed in their papers, manual efforts are extensively used to reconstruct images. For instance, both methods treat image color recovery as a separate task, by iterating multiple reconstruction trials and manually picking one with relatively better visual effect. Xu et al. (2015) exploit page table side channels and colors are rarely recovered. Hähnel et al. (2017) recover adequate image colors but only exploit finer-grained cache side channels. Also, domain-specific knowledge on `libjpeg` is required to locate a tiny portion of secret-dependent side channel signals for use. In contrast, we present an end-to-end approach to recovering colorful

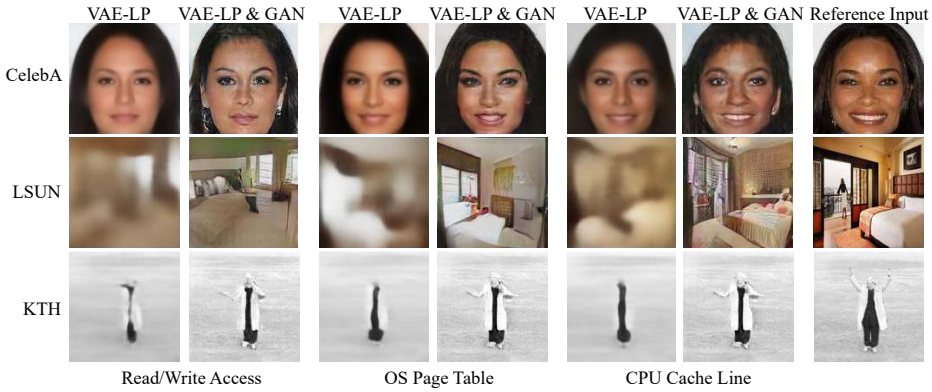

Figure 3: Qualitative evaluation results of three datasets in terms of three different side channels. Corresponding reference images (i.e., private user inputs) are presented on the rightmost column for comparison.

images with high quality, by directly analyzing a page table or cache side channel trace of up to 1.3M records. Our attack treats victim software (`libjpeg` or `uPNG`) as a "black-box" (no need for source code) and is independent of any underlying computing infrastructure details.

▪ **Benchmarks.** Three datasets are primarily used in the evaluation, containing typical daily images that could violate privacy if leaked to adversaries. Consistent with existing research reconstructing images from audio recording (Wen et al., 2019; Oh et al., 2019), we accelerate the model training using images of $3 \times 128 \times 128$ pixels. Wen et al. (2019) use images of an even smaller size ($3 \times 64 \times 64$). See Appendix B for model implementation and training details.

(i) Large-scale CelebFaces Attributes (CelebA) (Liu et al., 2015b) contains about 200K celebrity face images. We randomly select 80K images for training and 20K images for testing.

(ii) KTH Human Actions (KTH) (Laptev & Lindeberg, 2004) contains videos of six actions made by 25 persons in 4 directions. For each action, we randomly select videos of 20 persons for training and use the rest for testing. We have 40K images for training and 10K images for testing.

(iii) LSUN Bedroom Scene (LSUN) (Yu et al., 2015) contains images of typical bedroom scenes. We randomly select 80K images for training and 20K images for testing.

5.1 Qualitative Evaluation Results

Fig. 3 shows the reconstructed images in different settings. In addition to reporting the final outputs (i.e., the "VAE-LP & GAN" column), we also report images generated only from the VAE-LP module in the "VAE-LP" column for comparison. More results are given in Appendix C. For most of the cases, the reconstructed images and reference images show consistent visual appearances, such as gender, skin color, bedroom window, and human gesture. Images in the `LSUN` dataset contain many subtle bedroom details, imposing relatively higher challenge for reconstruction.

Realistic and recognizable images can be recovered using cache side channels (especially for `LSUN`) while images recovered from the other side channels are relatively blurry. As explained in Table 1, cache line indices ($addr \gg 6$) are closer to the memory address $addr$ (only missing the lowest 6 bits), while page table indices eliminate the lowest 12 bits from $addr$ (typically lower bits in $addr$ are informative and likely influenced by inputs), and each read/write pattern has only one bit.

Compared with images generated by VAE-LP, the GAN module enhances the image quality by adding details and sharpening the blurred regions. GAN may overly enhance the image quality (e.g., the first `LSUN` case with jungle green wallpaper). However, GAN is indeed vital to exploit user privacy. For example, considering the first human gesture case in `KTH`, where the image reconstructed from cache side channels contains a "black bar" when using VAE-LP. The GAN module enhances this obscure image and reconstructs the human gesture, thus violating user privacy.

5.2 Quantitative Evaluation Results

To assess the generated images w.r.t. discriminability, we first study the accuracy of matching a reconstructed image $\hat{i}$ to its reference input i. To do so, we form a set of N images which include the reference input i and $N-1$ images randomly selected from our testing dataset. We then measure

Table 2: Discriminability evaluation. We present success rates of random guess (RG) for the comparison.

	$k=1$ $N=100$				$k=5$ $N=100$				$k=20$ $N=100$			
	CelebA	KTH	LSUN	RG	CelebA	KTH	LSUN	RG	CelebA	KTH	LSUN	RG
CPU Cache Line	47.28%	38.22%	10.00%	1%	74.98%	63.56%	28.74%	5%	90.70%	83.72%	58.88%	20%
OS Page Table	16.16%	35.86%	2.26%	1%	37.96%	61.28%	8.62%	5%	65.14%	82.22%	26.42%	20%
Read/Write Pattern	19.58%	33.44%	2.24%	1%	42.44%	58.30%	8.28%	5%	67.82%	80.14%	26.64%	20%
	$k=1$ $N=500$				$k=5$ $N=500$				$k=20$ $N=500$			
	CelebA	KTH	LSUN	RG	CelebA	KTH	LSUN	RG	CelebA	KTH	LSUN	RG
CPU Cache Line	28.68%	24.50%	3.04%	0.2%	52.22%	41.24%	10.90%	1%	72.98%	61.08%	25.92%	4%
OS Page Table	6.56%	22.58%	0.46%	0.2%	17.90%	38.80%	2.42%	1%	35.22%	58.90%	7.30%	4%
Read/Write Pattern	8.42%	20.64%	0.50%	0.2%	21.18%	36.22%	2.54%	1%	39.84%	55.74%	7.08%	4%

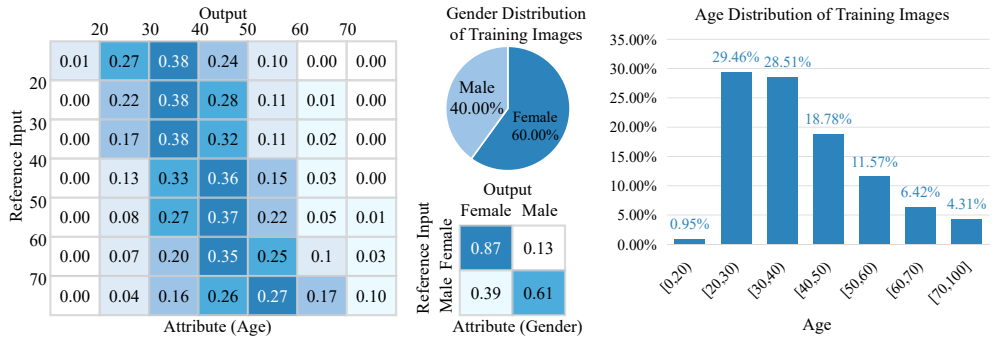

Figure 4: Facial attribute evaluation in terms of cache side channels. Confusion matrices (with row-wise normalization) compare the age and gender classification results on our recovered images and those obtained from reference inputs. We also report the age and gender distributions in the training set for the reference.

whether i appears in the top-k most similar images of $\hat{i}$. Conceptually, we mimic a de-anonymization attack of user identity, where N scopes the search space attackers are facing (e.g., all subscribers of a cloud service). We use a perceptually-based similarity metric, SSIM (Wang et al., 2004), to quantify structural-level similarity between the reconstructed images and reference inputs.

Table 2 reports the evaluation results of six practical settings. Consistent with Fig. 3, cache side channels help to reconstruct $\hat{i}$ with better discriminability (highest accuracy for all settings in Table 2). LSUN images have lower accuracy. As shown in Fig. 3, images in LSUN contain many subtle bedroom details and deem challenging for discrimination. We achieve the highest accuracy when $k = 20$ and $N = 100$, while the accuracy, as expected, decreases in more challenging settings (e.g., when $k = 1$ and $N = 500$). Evaluations consistently outperform the baseline — *random guess*. For instance, while the accuracy of random guess when $k = 1$ and $N = 500$ is 0.2%, we achieve higher accuracy (range from 0.46% to 28.68%) across all settings. Appendix D also conducts this evaluation using images generated from only VAE-LP. We report that better discriminability can be achieved for all datasets when supplementing VAE-LP with GAN.

For face images in CelebA, we also study how well different facial attributes are being captured in the reconstructed images. We use Face++ (fac, 2020), a commercial image analysis service, to classify reconstructed images and reference inputs w.r.t. age and gender attributes. Fig. 4 reports the confusion matrices for age and gender attributes and distributions of training data for the reference. The reconstructed images are produced using cache side channels. Overall, we achieve a good agreement for both male and female labels. We also observe correlated classification results for most age groups. The age distribution indicates that early adulthood (20–40) and middle age (40–60) mostly dominate the dataset, which presumably induces biases in the age confusion matrix. Similarly, "male" has a smaller representation in the training set, potentially explaining its lower agreement in the confusion matrix. Appendix D also conducts this evaluation using only VAE-LP or using other side channels where comparable results can be achieved.

5.3 Generalizability

This section explores the generalizability of our SCA. We launch attacks toward uPNG to illustrate that our method is *independent* of specific software implementation or image formats. For uPNG experiments, we evaluate attacks on the CelebA dataset using cache side channels. As shown

Table 3: Generalizability evaluation.

(k, N)	$(1, 100)$	$(5, 100)$	$(20, 100)$	$(1, 500)$	$(5, 500)$	$(20, 500)$
`uPNG`: SCA model trained with `CelebA`	18.8%	40.6%	66.0%	8.3%	20.7%	38.4%
`libjpeg`: SCA model trained with mini-Imagenet	4.4%	17.1%	39.8%	1.1%	5.0%	15.0%
Baseline — random guess	1%	5%	20%	0.2%	1%	4%

in table Table 3, our attack can recover discriminable images and largely outperforms the baseline (random guess) in terms of privacy inference. See Appendix E for the reconstructed images. We also benchmark our attack to synthesize arbitrary images without using *specific* types of images to train the model. We instead use a *general* training dataset, mini-Imagenet. We use cache side channels to exploit `libjpeg`. Table 3 illustrates that considerable privacy is leaked using mini-Imagenet as the training set, and for all settings, our SCA largely outperforms the baseline.

The recovered images when using mini-Imagenet as the training data are visually worse than images recovered using specialized datasets. See Appendix F for the recovered images. This observation reveals the potential *trade-off* of our research. Overall, training generative models using a general dataset without the knowledge of images classes seems "unconventional." A generative model is typically trained using dataset of only one class (Guo et al., 2019), or it requires image class information to be explicitly provided during both training and generation phases (Brock et al., 2019). Nevertheless, we still evaluate our approach using a general dataset to explore the *full potential* of our attack. We attribute the adequate results using general datasets to discriminable features extracted by our trace encoder from images of different classes. See Appendix G for further evaluations.

From a holistic perspective, the adopted training image sets constitute a *predictive model of user privacy*. While a particular user input is private, we assume that the functionality of victim software (e.g., a human face analysis service) is usually known to the public or can be probed prior to attacks.

6 Discussion

Better Side Channels. This is the first paper that provides a practical solution to reconstruct images from system side channels. Despite the encouraging results, the reconstructed images show room for improvement. For instance, not all image colors were well recovered. Our manual inspection shows that compared with `libjpeg`, `uPNG` does not impose informative side channel dependency on pixel colors (i.e., different colors can likely induce identical side channel logs). Nevertheless, user privacy is presumably leaked as long as the image skeleton is recovered. Colors (or other details) can be recovered if the system community discovered more powerful (finer-grained) side channels.

7 Related Work

System Side Channels. System side channels have been used to exploit various real-life software (Dong et al., 2018; Wu et al., 2012; Hähnel et al., 2017; Xu et al., 2015). The CPU cache is shown to be a rich source for SCA toward web browsers and cloud environments (Hähnel et al., 2017; Oren et al., 2015). In addition to cache line side channels analyzed in this research, other cache storage units, including cache bank and cache set, are also employed for SCA (Yarom et al., 2017; Liu et al., 2015a). Overall, while most attacks in this field perform dedicated SCA attacks toward specific side channels, our approach is general and orthogonal to particular side channels.

Profiling-based SCA. Machine learning has substantially boosted profiling-based SCA by learning from historical data. DNN models are used to recover secret keys from crypto libraries (Heuser & Zohner, 2012; Maghrebi et al., 2016; Cagli et al., 2017; Hettwer et al., 2018; Kim et al., 2019; Hettwer et al., 2020). However, their approaches primarily focus on classifying particular bits of crypto keys instead of holistically reconstructing and enhancing images.

8 Conclusion

This paper has presented a general and effective SCA framework. The framework is trained with side channels to exploit media software. Our evaluation shows that reconstructed images manifest close similarity with user inputs, making privacy leakage attacks practical. We also show surprising findings that enabled by our framework, attacks with low-resolution side channels become feasible.

REFERENCES

Face attributes analysis service. https://www.faceplusplus.com/attributes/, 2020.

PAGE MASK. https://elixir.bootlin.com/linux/v5.6.10/source/arch/x86/include/asm/page_types.h#L12, 2020.

Onur Aciicmez and Cetin Kaya Koc. Trace-driven cache attacks on AES. In *ICICS*, 2006.

Andrew Brock, Jeff Donahue, and Karen Simonyan. Large scale GAN training for high fidelity natural image synthesis. In *International Conference on Learning Representations*, 2019. URL https://openreview.net/forum?id=B1xsqj09Fm.

Eleonora Cagli, Cécile Dumas, and Emmanuel Prouff. Convolutional neural networks with data augmentation against jitter-based countermeasures. In *International Conference on Cryptographic Hardware and Embedded Systems*, pp. 45–68. Springer, 2017.

R. C. Chiang, S. Rajasekaran, N. Zhang, and H. H. Huang. Swiper: Exploiting virtual machine vulnerability in third-party clouds with competition for i/o resources. *IEEE Transactions on Parallel and Distributed Systems*, 26(6):1732–1742, June 2015. ISSN 1045-9219.

Alex Clark. Pillow. Python image analysis library, 2020. URL https://pillow.readthedocs.io/en/stable/.

Emily Denton and Rob Fergus. Stochastic video generation with a learned prior. In *International Conference on Machine Learning*, pp. 1174–1183, 2018.

Xiaowan Dong, Zhuojia Shen, John Criswell, Alan L Cox, and Sandhya Dwarkadas. Shielding software from privileged side-channel attacks. In *27th USENIX Security Symposium*, pp. 1441–1458, 2018.

Goran Doychev, Dominik Feld, Boris Kopf, Laurent Mauborgne, and Jan Reineke. CacheAudit: A tool for the static analysis of cache side channels. In *USENIX Sec.*, 2013.

David Gullasch, Endre Bangerter, and Stephan Krenn. Cache games—bringing access-based cache attacks on AES to practice. In *Proc. IEEE Symp. on Security and Privacy (S&P)*, pp. 490–505, 2011.

Yong Guo, Qi Chen, Jian Chen, Qingyao Wu, Qinfeng Shi, and Mingkui Tan. Auto-embedding generative adversarial networks for high resolution image synthesis. *IEEE Transactions on Multimedia*, 21(11):2726–2737, 2019.

Marcus Hähnel, Weidong Cui, and Marcus Peinado. High-resolution side channels for untrusted operating systems. In *2017 USENIX Annual Technical Conference*, pp. 299–312, 2017.

Y. Han, J. Chan, T. Alpcan, and C. Leckie. Using virtual machine allocation policies to defend against co-resident attacks in cloud computing. *IEEE Transactions on Dependable and Secure Computing*, 14:95–108, Jan 2017.

Benjamin Hettwer, Stefan Gehrer, and Tim Güneysu. Profiled power analysis attacks using convolutional neural networks with domain knowledge. In *International Conference on Selected Areas in Cryptography*, pp. 479–498. Springer, 2018.

Benjamin Hettwer, Tobias Horn, Stefan Gehrer, and Tim Güneysu. Encoding power traces as images for efficient side-channel analysis. *arXiv preprint arXiv:2004.11015*, 2020.

Annelie Heuser and Michael Zohner. Intelligent machine homicide. In *International Workshop on Constructive Side-Channel Analysis and Secure Design*, pp. 249–264. Springer, 2012.

Sanghyun Hong, Michael Davinroy, Yiğitcan Kaya, Stuart Nevans Locke, Ian Rackow, Kevin Kulda, Dana Dachman-Soled, and Tudor Dumitraş. Security analysis of deep neural networks operating in the presence of cache side-channel attacks. *arXiv preprint arXiv:1810.03487*, 2018a.

Sanghyun Hong, Michael Davinroy, Yiğitcan Kaya, Dana Dachman-Soled, and Tudor Dumitraş. How to 0wn the nas in your spare time. In *International Conference on Learning Representations*, 2020. URL https://openreview.net/forum?id=S1erpeBFPB.

Seunghoon Hong, Dingdong Yang, Jongwook Choi, and Honglak Lee. Inferring semantic layout for hierarchical text-to-image synthesis. In *Proceedings of the IEEE Conference on Computer Vision and Pattern Recognition*, pp. 7986–7994, 2018b.

Gabriel Hospodar, Benedikt Gierlichs, Elke De Mulder, Ingrid Verbauwhede, and Joos Vandewalle. Machine learning in side-channel analysis: a first study. *Journal of Cryptographic Engineering*, 1(4):293, 2011.

Intel. Intel software guard extensions programming reference. https://software.intel.com/sites/default/files/managed/48/88/329298-002.pdf/, 2014. Order Number: 329298-002, October 2014.

Jaehun Kim, Stjepan Picek, Annelie Heuser, Shivam Bhasin, and Alan Hanjalic. Make some noise. unleashing the power of convolutional neural networks for profiled side-channel analysis. *IACR Transactions on Cryptographic Hardware and Embedded Systems*, pp. 148–179, 2019.

Diederik P. Kingma and Jimmy Ba. Adam: A method for stochastic optimization, 2014.

Ivan Laptev and Tony Lindeberg. Velocity adaptation of space-time interest points. In *Proceedings of the 17th International Conference on Pattern Recognition, 2004. ICPR 2004.*, volume 1, pp. 52–56. IEEE, 2004.

libjpeg. Main libjpeg-turbo repository, 2020. URL https://github.com/libjpeg-turbo/libjpeg-turbo.

Fangfei Liu, Y. Yarom, Qian Ge, G. Heiser, and R.B. Lee. Last-level cache side-channel attacks are practical. In *2015 IEEE Symposium on Security and Privacy*, pp. 605–622, May 2015a.

Ziwei Liu, Ping Luo, Xiaogang Wang, and Xiaoou Tang. Deep learning face attributes in the wild. In *Proceedings of International Conference on Computer Vision (ICCV)*, December 2015b.

Chi-Keung Luk, Robert Cohn, Robert Muth, Harish Patil, Artur Klauser, Geoff Lowney, Steven Wallace, Vijay Janapa Reddi, and Kim Hazelwood. Pin: building customized program analysis tools with dynamic instrumentation. In *Proceedings of the 2005 ACM SIGPLAN conference on Programming language design and implementation (PLDI'05)*, 2005.

Houssem Maghrebi, Thibault Portigliatti, and Emmanuel Prouff. Breaking cryptographic implementations using deep learning techniques. In *International Conference on Security, Privacy, and Applied Cryptography Engineering*, pp. 3–26. Springer, 2016.

Sean Middleditch. upng, 2010. URL https://github.com/elanthis/upng.

Tae-Hyun Oh, Tali Dekel, Changil Kim, Inbar Mosseri, William T Freeman, Michael Rubinstein, and Wojciech Matusik. Speech2face: Learning the face behind a voice. In *Proceedings of the IEEE Conference on Computer Vision and Pattern Recognition*, pp. 7539–7548, 2019.

Yossef Oren, Vasileios P Kemerlis, Simha Sethumadhavan, and Angelos D Keromytis. The spy in the sandbox: Practical cache attacks in javascript and their implications. In *Proceedings of the 22nd ACM SIGSAC Conference on Computer and Communications Security*, pp. 1406–1418, 2015.

Alec Radford, Luke Metz, and Soumith Chintala. Unsupervised representation learning with deep convolutional generative adversarial networks. In *Proceedings of 4th International Conference on Learning Representations*, 2016.

Scott Reed, Zeynep Akata, Xinchen Yan, Lajanugen Logeswaran, Bernt Schiele, and Honglak Lee. Generative adversarial text to image synthesis. In *International Conference on Machine Learning*, 2016.

Shuai Wang, Pei Wang, Xiao Liu, Danfeng Zhang, and Dinghao Wu. CacheD: Identifying cache-based timing channels in production software. In *26th USENIX Security Symposium*, pp. 235–252, 2017.

Zhou Wang, Alan C Bovik, Hamid R Sheikh, and Eero P Simoncelli. Image quality assessment: from error visibility to structural similarity. *IEEE transactions on image processing*, 13(4):600–612, 2004.

Yandong Wen, Bhiksha Raj, and Rita Singh. Face reconstruction from voice using generative adversarial networks. In *Advances in Neural Information Processing Systems*, pp. 5266–5275, 2019.

Zhenyu Wu, Zhang Xu, and Haining Wang. Whispers in the hyper-space: High-speed covert channel attacks in the cloud. In *Presented as part of the 21st USENIX Security Symposium (USENIX Security 12)*, pp. 159–173, 2012.

Yuanzhong Xu, Weidong Cui, and Marcus Peinado. Controlled-channel attacks: Deterministic side channels for untrusted operating systems. In *2015 IEEE Symposium on Security and Privacy*, pp. 640–656. IEEE, 2015.

Yuval Yarom and Katrina Falkner. FLUSH+RELOAD: A high resolution, low noise, L3 cache side-channel attack. In *Proceedings of the 23rd USENIX Conference on Security Symposium*, pp. 719–732, 2014.

Yuval Yarom, Daniel Genkin, and Nadia Heninger. Cachebleed: a timing attack on openssl constant-time rsa. *Journal of Cryptographic Engineering*, 7(2):99–112, 2017.

Fisher Yu, Ari Seff, Yinda Zhang, Shuran Song, Thomas Funkhouser, and Jianxiong Xiao. LSUN: Construction of a large-scale image dataset using deep learning with humans in the loop. *arXiv preprint arXiv:1506.03365*, 2015.

A ATTACK SETUP DETAILS

In this section, we provide detailed information regarding our attack setup, including three employed side channels, the attacked `libjpeg` and `uPNG` libraries (libjpeg, 2020; Middleditch, 2010), and how we log side channel signals. Three side channels are taken into account as follows:

- **Cache Line.** Cache line side channel denotes one popular hardware side channel, enabling the exploitation of real-world crypto, image and text libraries (Hähnel et al., 2017; Yarom & Falkner, 2014). The CPU cache, as one key component in modern computer architecture, stores data so that future memory requests of that particular data become much faster. Data are stored in a cache block of fixed size, called the cache line. Each memory access made by victim software is projected to a cache line access. In typical cloud platforms, an attacker can monitor cache line accesses made by victim software, leading to a powerful side channel. For modern Intel architectures, the cache line index of a memory address $addr$ can be computed as $addr \gg 6$. Therefore, access of a particular cache line can be mapped back to 2^6 memory addresses.
- **Page Table.** The OS kernel uses the page table to track mappings between virtual and physical memory addresses. Every memory access made by the victim software is converted into its physical address by querying a page table entry. In cloud computing platforms, a malicious OS on the host can observe page table accesses made by the victim software to infer its memory access (Xu et al., 2015). Given a virtual address $addr$, we calculate the accessed page table index by masking $addr$ with `PAGE_MASK` M: $addr \,\&\, (\sim M)$. M is 4095 on modern x86 architectures (pag, 2020).
- **Data Read/Write Access.** Our preliminary study shows surprising results that enabled by powerful generative models, low-resolution side channels of only one-bit data read/write access records can be used to recover quality images. That is, given a memory access made by the victim software, we use one bit to note whether the access is a read or write operation. Such data read/write accesses can be easily observed by monitoring either cache or page table accesses.

SCA attacks using cache lines and page tables are well-known and have enabled real-life exploitations in various scenarios. In contrast, to our knowledge, no real-world attacks are designed to exploit read/write patterns. This work shows that quality images can be synthesized by using such low-resolution read/write access side channels.

Preparing Victim Software Consistent with existing SCA of exploiting media software (Xu et al., 2015; Hähnel et al., 2017), we use a widely-used JPEG image processing library, `libjpeg`, as the attack target. Attacking `libjpeg` which has been exploited in the literatures makes it easier to (conceptually) compare our approach with existing works. As mentioned in our paper, we indeed contact authors of both papers to inquire their tools; we didn't receive any response by the time of writing. As disclosed in their papers, *manual efforts* are primarily used to recover images. On the other hand, there is **no** issue for our approach to analyze other image processing libraries as long as different inputs adequately influence side channel logs. To demonstrate the *generalizability* of our approach, we also attacked another image library, `uPNG`, which takes images of PNG format as the inputs.

JPEG and PNG are two popular image compression standards. Given an image of JPEG/PNG formats, both image processing libraries reverse the compression step to generate a bitmap image as the prerequisite of many image analysis applications. The decompression process introduces considerable amount of input-dependent side channel accesses for both libraries. We compile both `libjpeg` and `uPNG` on 64-bit Ubuntu 18.04 machine with `gcc` with optimization-level as `-O0` which disables all optimizations.

We measure the complex of `libjpeg`, by counting the line of code of the attacked `libjpeg` module. We report the attacked module, conducting JPEG image decompression under various settings, has approximately 46K lines of code. Similarly, the `uPNG` software has about 1.2K lines of code. In contrast, typically the crypto software attacked by previous profiling-based SCA (Hettwer et al., 2020; Gullasch et al., 2011; Aciicmez & Koc, 2006; Yarom et al., 2017) are much simpler. For

instance, the x86 implementation of Advanced Encryption Standard (AES) in `OpenSSL` has about 600 lines of code (excluding global data structures like permutation boxes).

Preparing Side Channel Logs To prepare side channel traces, we use `Pin` (Luk et al., 2005), a runtime monitoring framework developed by Intel to intercept all memory accesses of our test programs when processing an input image i. Every virtual address $addr$ on the logged trace is translated into its corresponding cache line and page table indexes following the aforementioned methods. Similarly, we intercept all memory accesses, and for each memory access, we use one bit to denote whether it is a data read or write access. All these runtime monitoring tasks can be done by writing two plugins of `Pin`. We report that processing each image with `libjpeg` can generate a trace of 730K to 760K side channel records. Processing an image with `uPNG` can generate a trace of about 1.3M side channel records. Recall as introduced in Sec. 3.1, each side channel trace is encoded into a $N \times N \times K$ matrix and then processed by CNNs. A `libjpeg` trace is encoded into a $512 \times 512 \times 3$ matrix. A `uPNG` trace is encoded into a $512 \times 512 \times 6$ matrix. We do zero padding for matrices. In comparison, exploiting crypto libraries (e.g., AES decryption) generates much succinct side channel traces with only a few hundred records (Hettwer et al., 2020),

Attacking Other Image Processing Software and DNN Models We pick `libjpeg` since this is the *only* media software attacked by existing SCA (Xu et al., 2015; Hähnel et al., 2017). We also attacked `uPNG` to demonstrate the generalizability of our approach. Note that `libjpeg` is commonly used in the image analysis pipeline, e.g., it is the prerequisite of the popular Python image processing library — `Pillow` (Clark, 2020).

Also, careful readers may wonder the feasibility of directly exploiting DNN-based image analysis tools. However, as pointed out in previous research (Hong et al., 2018a), memory access of typical DNN operations like matrix multiplications is **not** input-dependent. That is, while it has been demonstrated by the same authors that cache side channels is feasible to recover DNN model architectures (Hong et al., 2020), SCA is generally **not** feasible to recover inputs to DNN models.

B MODEL ARCHITECTURE AND EXPERIMENT SETUP

We now report the architecture and parameters of our framework. The Enc_{trace} of VAE-LP module is reported in Table 5. Enc_{image} and Dec_{image} are reported in Table 4. The generator G and discriminator D of our GAN module are listed in Table 6 and Table 7, respectively.

We implement our framework in Pytorch (ver. 1.5.0). We use the Adam optimizer (Kingma & Ba, 2014) with learning rate $\eta_{VAE-LP} = 0.0001$ for the VAE-LP module, and learning rate $\eta_{GAN} = 0.0002$ for the GAN module. We set $\beta_1 = 0.5$, and $\beta_2 = 0.999$ for both modules. β in $Loss_{VAE-LP}$ is 0.0001, and γ in $Loss_{GAN}$ is 100. Minibatch size is 50.

We ran our experiments on an Intel Xeon CPU E5-2678 with 256 GB of RAM and one Nvidia GeForce RTX 2080 GPU. The training is completed at 200 iterations (100 iterations for the VAE-LP module, and 100 iterations for the GAN module).

Table 4: The image encoder Enc_{image} and image decoder Dec_{image} architectures.

Image Encoder			Image Decoder		
Layer	Act.	Output shape	Layer	Act.	Output shape
Input	-	$3 \times 128 \times 128$	Input	-	$128 \times 1 \times 1$
Conv $4 \times 4_{/2,1}$	LReLU(0.2)	$128 \times 64 \times 64$	Deconv $4 \times 4_{/1,0}$	BN + ReLU	$128 \times 4 \times 4$
ResBlock (**?**)	-	$128 \times 64 \times 64$	ResBlock	-	$128 \times 4 \times 4$
Conv $4 \times 4_{/2,1}$	BN + LReLU(0.2)	$128 \times 32 \times 32$	Deconv $4 \times 4_{/2,1}$	BN + ReLU	$128 \times 8 \times 8$
ResBlock	-	$128 \times 32 \times 32$	ResBlock	-	$128 \times 8 \times 8$
Conv $4 \times 4_{/2,1}$	BN + LReLU(0.2)	$128 \times 16 \times 16$	Deconv $4 \times 4_{/2,1}$	BN + ReLU	$128 \times 16 \times 16$
ResBlock	-	$128 \times 16 \times 16$	ResBlock	-	$128 \times 16 \times 16$
Conv $4 \times 4_{/2,1}$	BN + LReLU(0.2)	$128 \times 8 \times 8$	Deconv $4 \times 4_{/2,1}$	BN + ReLU	$128 \times 32 \times 32$
ResBlock	-	$128 \times 8 \times 8$	ResBlock	-	$128 \times 32 \times 32$
Conv $4 \times 4_{/2,1}$	BN + LReLU(0.2)	$128 \times 4 \times 4$	Deconv $4 \times 4_{/2,1}$	BN + ReLU	$128 \times 64 \times 64$
ResBlock	-	$128 \times 4 \times 4$	ResBlock	-	$128 \times 64 \times 64$
Conv $4 \times 4_{/1,0}$	LReLU(0.2)	$128 \times 1 \times 1$	Deconv $4 \times 4_{/2,1}$	Tanh	$3 \times 128 \times 128$
Output	-	128	Output	-	$3 \times 128 \times 128$

Table 5: The trace encoder Enc_{trace} architecture.

Trace Encoder		
Layer	Act.	Output shape
Input	-	$3 \times 512 \times 512$
Normalize	-	$3 \times 512 \times 512$
Conv $4 \times 4_{/2,1}$	BN + LReLU(0.2)	$64 \times 256 \times 256$
Conv $4 \times 4_{/2,1}$	BN + LReLU(0.2)	$64 \times 128 \times 128$
Conv $4 \times 4_{/2,1}$	BN + LReLU(0.2)	$64 \times 64 \times 64$
Conv $4 \times 4_{/2,1}$	BN + LReLU(0.2)	$128 \times 32 \times 32$
Conv $4 \times 4_{/2,1}$	BN + LReLU(0.2)	$256 \times 16 \times 16$
Conv $4 \times 4_{/2,1}$	BN + LReLU(0.2)	$512 \times 8 \times 8$
Conv $4 \times 4_{/2,1}$	BN + LReLU(0.2)	$512 \times 4 \times 4$
Conv $4 \times 4_{/1,0}$	BN + Tanh	$128 \times 1 \times 1$
Output	-	128

Table 6: The generator G architecture.

Encoder			Decoder		
Layer	Act.	Output shape	Layer	Act.	Output shape
Input	-	$3 \times 128 \times 128$	Input	-	$1024 \times 1 \times 1$
Conv $4 \times 4_{/2,1}$	-	$128 \times 64 \times 64$	Deconv $4 \times 4_{/2,1}$	BN + ReLU	$1024 \times 2 \times 2$
Conv $4 \times 4_{/2,1}$	BN + LReLU(0.2)	$256 \times 32 \times 32$	Deconv $4 \times 4_{/2,1}$	BN + ReLU	$1024 \times 4 \times 4$
Conv $4 \times 4_{/2,1}$	BN + LReLU(0.2)	$512 \times 16 \times 16$	Deconv $4 \times 4_{/2,1}$	BN + ReLU	$1024 \times 8 \times 8$
Conv $4 \times 4_{/2,1}$	BN + LReLU(0.2)	$1024 \times 8 \times 8$	Deconv $4 \times 4_{/2,1}$	BN + ReLU	$512 \times 16 \times 16$
Conv $4 \times 4_{/2,1}$	BN + LReLU(0.2)	$1024 \times 4 \times 4$	Deconv $4 \times 4_{/2,1}$	BN + ReLU	$256 \times 32 \times 32$
Conv $4 \times 4_{/2,1}$	BN + LReLU(0.2)	$1024 \times 2 \times 2$	Deconv $4 \times 4_{/2,1}$	BN + ReLU	$128 \times 64 \times 64$
Conv $4 \times 4_{/2,1}$	LReLU(0.2)	$1024 \times 1 \times 1$	Deconv $4 \times 4_{/2,1}$	Tanh	$3 \times 128 \times 128$
Output	-	$1024 \times 1 \times 1$	Output	-	$3 \times 128 \times 128$

Table 7: The discriminator D architecture.

Discriminator		
Layer	Act.	Output shape
Input	-	$3 \times 128 \times 128$
Conv $4 \times 4_{/2,1}$	BN + LReLU(0.2)	$128 \times 64 \times 64$
Conv $4 \times 4_{/2,1}$	BN + LReLU(0.2)	$256 \times 32 \times 32$
Conv $4 \times 4_{/2,1}$	BN + LReLU(0.2)	$512 \times 16 \times 16$
Conv $4 \times 4_{/2,1}$	BN + LReLU(0.2)	$1024 \times 8 \times 8$
Conv $4 \times 4_{/2,1}$	BN + LReLU(0.2)	$1024 \times 4 \times 4$
Conv $4 \times 4_{/1,0}$	Sigmoid	$1 \times 1 \times 1$
Output	-	1

C SAMPLE OUTPUTS WHEN ATTACKING LIBJPEG

This section provides more images generated by our framework when attacking `libjpeg`. Overall, we interpret the results as promising and highly consistent across all three different datasets. As discussed in Sec. 5.1, the reconstructed and the corresponding reference images show highly consistent identities, such as gender, face orientation, human gesture, and hair style.

Figure 5: Evaluation results of `CelebA` dataset in terms of three different side channel signals. The reference images (i.e., private user inputs) are presented on the right most column for the reference.

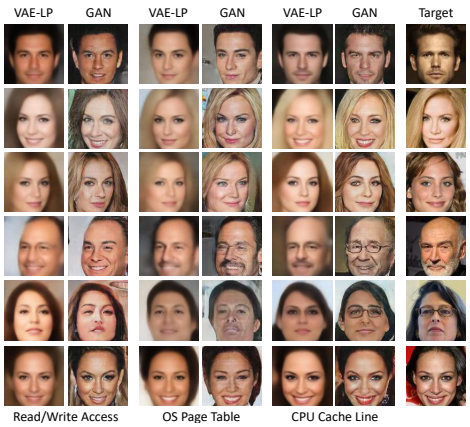

Figure 6: Evaluation results of `CelebA` dataset in terms of three different side channel signals. The reference images (i.e., private user inputs) are presented on the right most column for the reference.

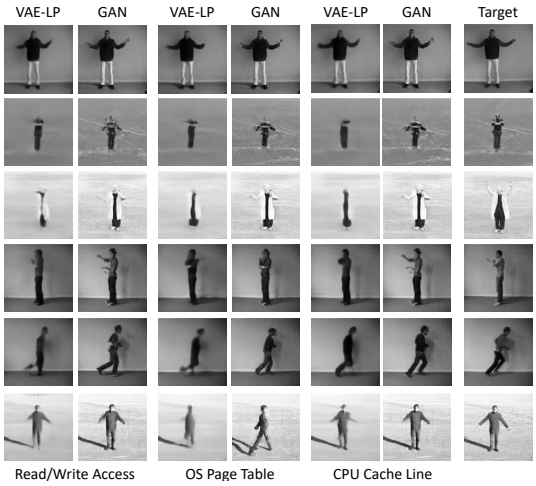

Figure 7: Evaluation results of KTH dataset in terms of three different side channel signals. The reference images (i.e., private user inputs) are presented on the right most column for the reference.

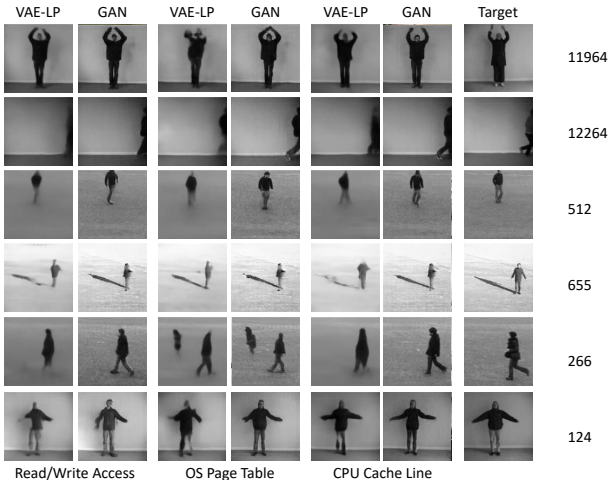

Figure 8: Evaluation results of KTH dataset in terms of three different side channel signals. The reference images (i.e., private user inputs) are presented on the right most column for the reference.

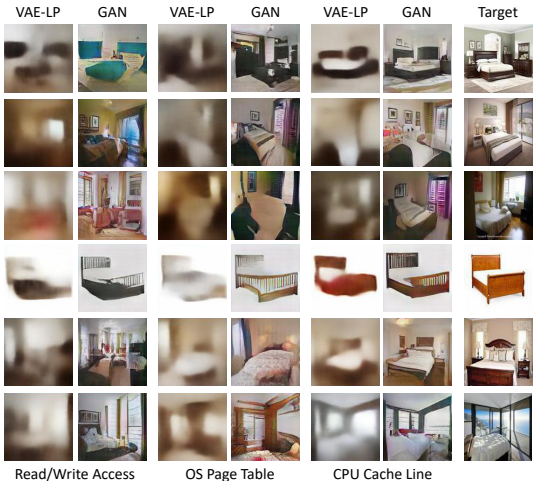

Figure 9: Evaluation results of LSUN dataset in terms of three different side channel signals. The reference images (i.e., private user inputs) are presented on the right most column for the reference.

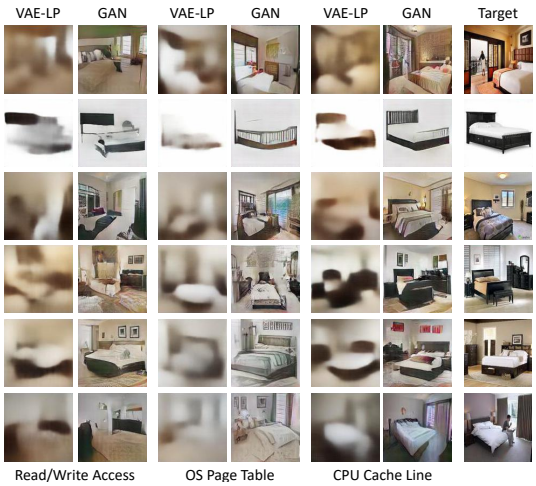

Figure 10: Evaluation results of LSUN dataset in terms of three different side channel signals. The reference images (i.e., private user inputs) are presented on the right most column for the reference.

D QUANTITATIVE EVALUATION

Besides the quantitative evaluation of the discriminability of reconstructed images reported in the paper, we also analyze images reconstructed by using only the VAE-LP module and presented the results in Table 8. Accordingly, we give the quantitative data that has been already reported in our paper for cross comparison in Table 9.

Table 8: Discriminability evaluation results on outputs using VAE-LP (higher is better). We also present the baseline, random guess (RG), for comparison.

	$k = 1$ $N = 100$				$k = 1$ $N = 500$			
	CelebA	KTH	LSUN	RG	CelebA	KTH	LSUN	RG
Cache Line	49.98%	30.28%	10.36%	1%	31.18%	19.82%	3.30%	0.2%
Page Table	14.66%	29.00%	1.94%	1%	5.98%	18.20%	0.50%	0.2%
Read/Write	17.52%	24.46%	1.98%	1%	7.86%	14.92%	0.40%	0.2%
	$k = 5$ $N = 100$				$k = 5$ $N = 500$			
	CelebA	KTH	LSUN	RG	CelebA	KTH	LSUN	RG
Cache Line	78.00%	54.42%	29.74%	5%	56.06%	32.86%	11.50%	1%
Page Table	35.38%	52.70%	7.92%	5%	16.92%	31.54%	1.92%	1%
Read/Write	39.16%	47.06%	7.08%	5%	19.68%	26.02%	1.86%	1%
	$k = 20$ $N = 100$				$k = 20$ $N = 500$			
	CelebA	KTH	LSUN	RG	CelebA	KTH	LSUN	RG
Cache Line	91.98%	79.16%	59.66%	20%	75.98%	51.20%	26.72%	4%
Page Table	61.94%	76.88%	24.90%	20%	32.96%	50.32%	6.48%	4%
Read/Write	65.46%	72.92%	24.56%	20%	36.90%	43.78%	6.30%	4%

Table 9: Discriminability evaluation results on the outputs using VAE-LP & GAN modules (higher is better). We have already reported these results in Table 2.

	$k = 1$ $N = 100$				$k = 1$ $N = 500$			
	CelebA	KTH	LSUN	RG	CelebA	KTH	LSUN	RG
Cache Line	47.28%	38.22%	10.00%	1%	28.68%	24.50%	3.04%	0.2%
Page Table	16.16%	35.86%	2.26%	1%	6.56%	22.58%	0.46%	0.2%
Read/Write	19.58%	33.44%	2.24%	1%	8.42%	20.64%	0.50%	0.2%
	$k = 5$ $N = 100$				$k = 5$ $N = 500$			
	CelebA	KTH	LSUN	RG	CelebA	KTH	LSUN	RG
Cache Line	74.98%	63.56%	28.74%	5%	52.22%	41.24%	10.90%	1%
Page Table	37.96%	61.28%	8.62%	5%	17.90%	38.80%	2.42%	1%
Read/Write	42.44%	58.30%	8.28%	5%	21.18%	36.22%	2.54%	1%
	$k = 20$ $N = 100$				$k = 20$ $N = 500$			
	CelebA	KTH	LSUN	RG	CelebA	KTH	LSUN	RG
Cache Line	90.70%	83.72%	58.88%	20%	72.98%	61.08%	25.92%	4%
Page Table	65.14%	82.22%	26.42%	20%	35.22%	58.90%	7.30%	4%
Read/Write	67.82%	80.14%	26.64%	20%	39.84%	55.74%	7.08%	4%

Comparing results reported in Table 8 and Table 9, we observed that by using VAE-LP & GAN modules together, the KTH human gesture dataset has a substantial improvement in terms of accuracy. The average accuracy of the KTH dataset is 41.9% in Table 8 while the average accuracy of the KTH dataset is increased to 49.8% in Table 9. This observation is consistent with our findings in Sec. 5.2 and some cases demonstrated in Fig. 7 and Fig. 8. Recall we observed an obscure "black bar" in KTH images reconstructed by only using VAE-LP module, while a human gesture can be clearly identified by enhancing the "black bar" with the GAN module. We also observed improved accuracy for the CelebA (41.0% to 41.4%) and LSUN datasets (12.6% to 12.9%) when supplementing VAE-LP with GAN. Overall, we interpret that better discriminability can be achieved when using GAN, implying higher success rate for attackers to de-anonymize user identity and privacy.

We also present fine-grained facial attribute comparison between the reconstructed images and reference inputs. In Sec. 5.2 we have reported gender and age confusion matrices evaluation using cache side channels (also presented in Fig. 11 for the reference and cross comparison), we also report other settings in Fig. 12, Fig. 13, and Fig. 14. To quantitatively evaluate the confusion matrices, we measure and report the weighted-average F1 score in Table 10. Besides one case with notably increased F1 score (the gender matrix using page table), VAE-LP and VAE-LP & GAN have comparable weighted-average F1 scores.

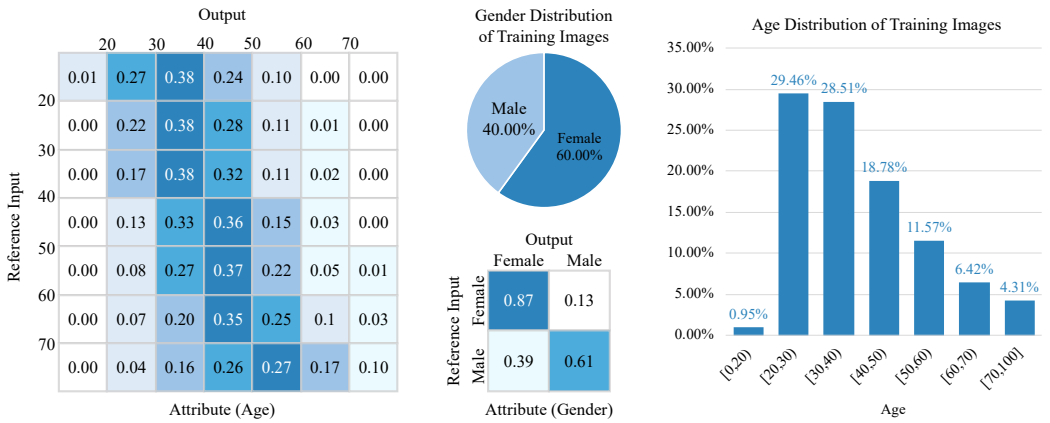

Figure 11: Facial attribute evaluation in terms of cache side channels. Images are generated using VAE-LP & GAN modules. Confusion matrices (with row-wise normalization) compare the age and gender classification results on our recovered images and those obtained from reference inputs. We also report age and gender distribution in the dataset for comparison. We have already reported these results in Fig. 4.

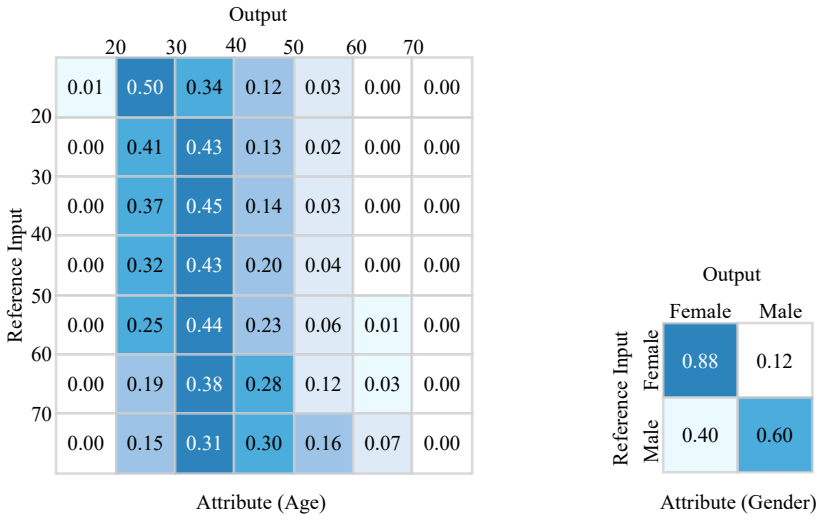

Figure 12: Facial attribute evaluation in terms of cache side channels. Images are generated using the VAE-LP module. Confusion matrices (with row-wise normalization) compare the age and gender classification results on our recovered images and those obtained from reference inputs. The age and gender distributions in the dataset have been given in Fig. 11.

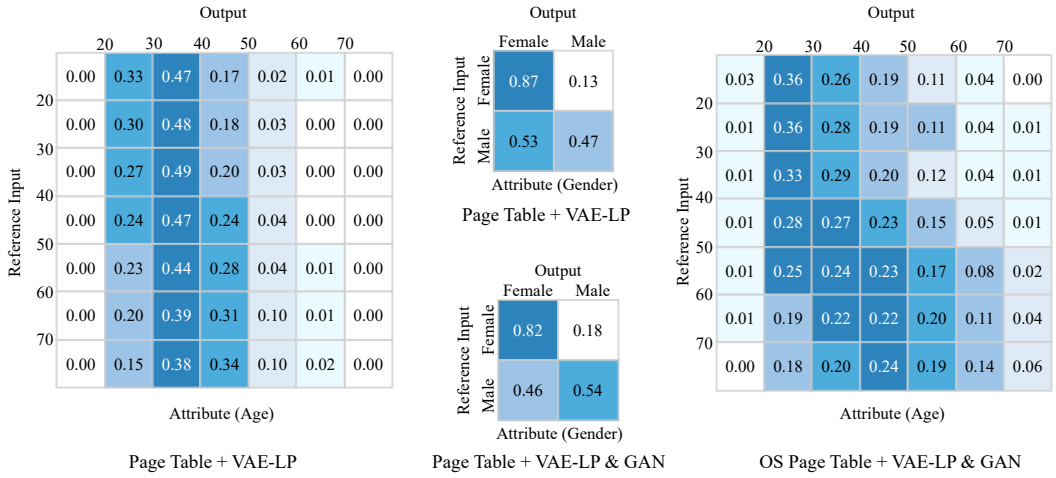

Figure 13: Facial attribute evaluation in terms of page table side channels. We present evaluation results by using images reconstructed using only VAE-LP module, and images reconstructed using VAE-LP & GAN. Confusion matrices (with row-wise normalization) compare the age and gender classification results on our recovered images and those obtained from reference inputs. The age and gender distribution in the dataset have been given in Fig. 11.

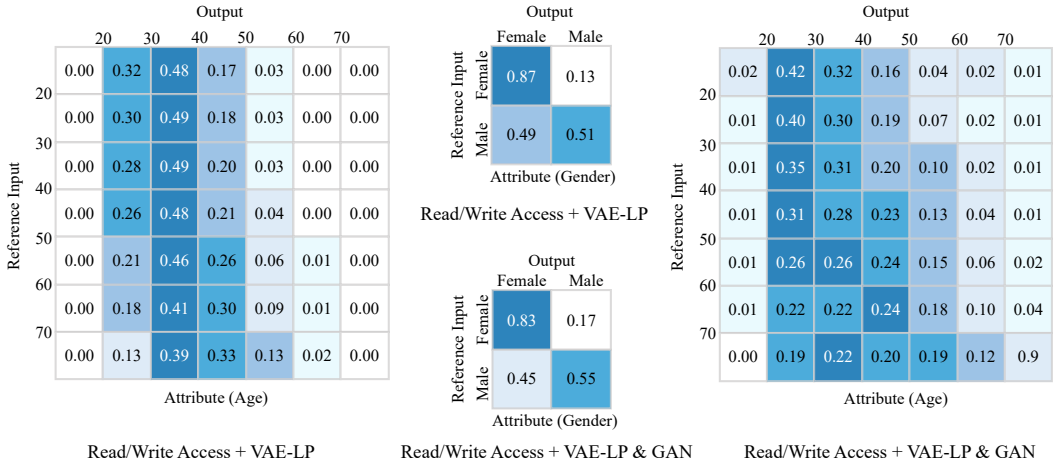

Figure 14: Facial attribute evaluation in terms of memory read/write access pattern side channels. We present evaluation results by using images reconstructed using only VAE-LP module, and images reconstructed using VAE-LP & GAN. Confusion matrices (with row-wise normalization) compare the age and gender classification results on our recovered images and those obtained from reference inputs. The age and gender distribution in the dataset have been given in Fig. 11.

Table 10: Weighted-average F1-score (higher is better).

	Age		Gender	
	VAE-LP	VAE-LP & GAN	VAE-LP	VAE-LP & GAN
CPU Cache Line	0.27	0.27	0.76	0.75
OS Page Table	0.25	0.26	0.68	0.79
Memory Read/Write	0.25	0.27	0.71	0.71

E SAMPLE OUTPUTS WHEN ATTACKING uPNG

This section provides images generated by our framework when attacking uPNG. While the side channel traces induced by uPNG is generally less informative than libjpeg (as shown in Table 3 and discussed in Sec. 6), we still observed high visually consistent identities between the reconstructed images and their reference inputs, including gender, face orientation, hair style, hair length, whether wearing a pair of glasses and many other factors.

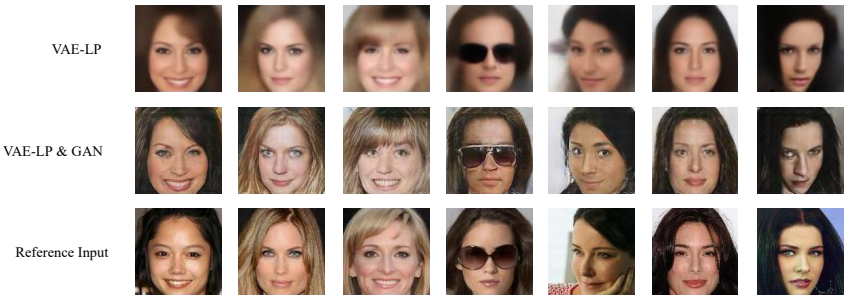

Figure 15: Evaluation results of CelebA dataset in terms of the cache side channels.

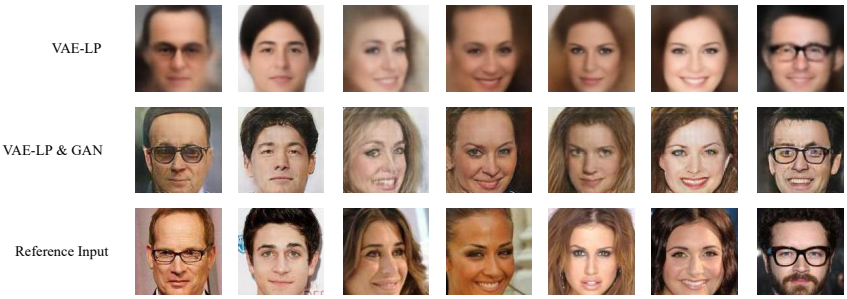

Figure 16: Evaluation results of CelebA dataset in terms of the cache side channels.

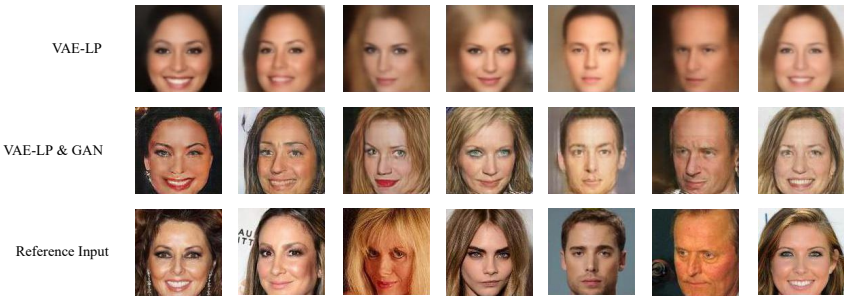

Figure 17: Evaluation results of CelebA dataset in terms of the cache side channels.

F SAMPLE OUTPUTS WHEN TRAINING WITH MINI-IMAGENET

To measure our attack reconstructing arbitrary images without knowing the type of images being processed, Sec. 5.3 reports model training and attack performance using a general dataset, mini-Imagenet. We report that the mini-Imagenet dataset has in total 60K images of 100 classes, and we divide each class (with 600 images) into 480 training images and 120 testing images. As a result, we have in total 48K images for training and take the other 12K images for testing. While training generative models with a general dataset is not the common practice unless image class information is explicitly provided (Brock et al., 2019), Table 3 still reports highly encouraging results of the discriminability analysis by largely outperforming the baseline — random guess. In this section, we provide sample images generated at this step.

The synthesized images from the mini-Imagenet dataset is visually much worse that images synthesized from specific datasets (e.g., `CelebA` in Fig. 5). Nevertheless, by comparing the synthesized images and their corresponding references (i.e., user inputs), we interpret that images still exhibit high discriminability, in the sense that many visually consistent image skeletons and colors are recovered, indicating adequate leakage of user privacy.

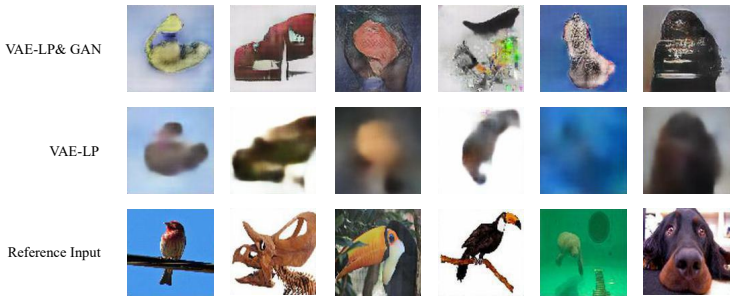

Figure 18: Evaluation results of mini-Imagenet dataset when attacking `libjpeg` with cache side channels.

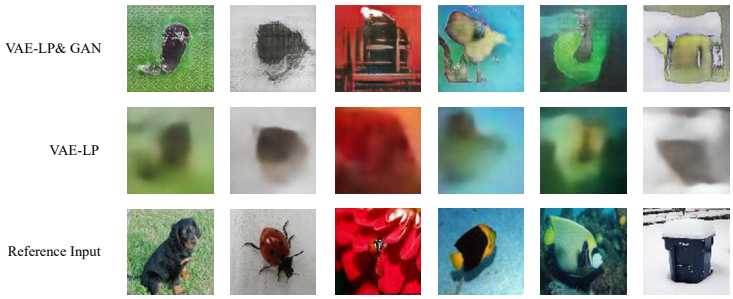

Figure 19: Evaluation results of mini-Imagenet dataset when attacking `libjpeg` with cache side channels.

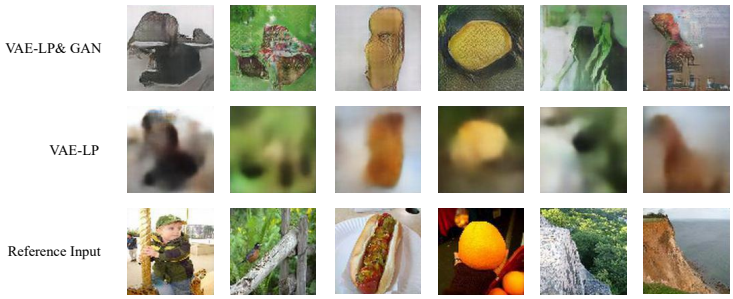

Figure 20: Evaluation results of mini-Imagenet dataset when attacking `libjpeg` with cache side channels.

G Classifying Outputs of The Trace Encoder

By training our framework with mini-Imagenet and assessing the discriminability, Sec. 5.3 has demonstrated that our attack can largely outperform the baseline even with no prior knowledge on the class information of user private images. We attribute the promising evaluation results to the discriminable features successfully extracted by our trace encoder (trained with mini-Imagenet; see Appendix F). This section presents empirical results by assessing to what extent the latent representations derived from images of two randomly selected classes are distinguishable.

To this end, we build a binary classifier, by piggybacking our trace encoder with a fully-connected (FC) layer and using Sigmoid as the activation function. As mentioned in Appendix F, the mini-Imagenet dataset has in total 60K images of 100 classes, and we divide each class into 480 images for training and 120 images for testing. At this step, we randomly select two classes of images, and use their training sets (in total 960 images) to train the proposed binary classifier. We then use their testing sets, including in total 240 images, to measure the binary classification accuracy. It is worth mentioning that we only train the classifier for one epoch to highlight that the latent representations extracted by the trace encoder already exhibit high quality and discriminability. We only tune the parameters of FC layer but preserve the parameters of our trace encoder.

We iterate this process for 100 times. Fig. 21 reports the classification accuracy across all 100 binary classification tasks. While the baseline accuracy for our binary classification task is 50%, most tasks exhibit much higher classification accuracy. We report the average accuracy is 81.6% and 32 cases exhibit a classification accuracy above 90%.

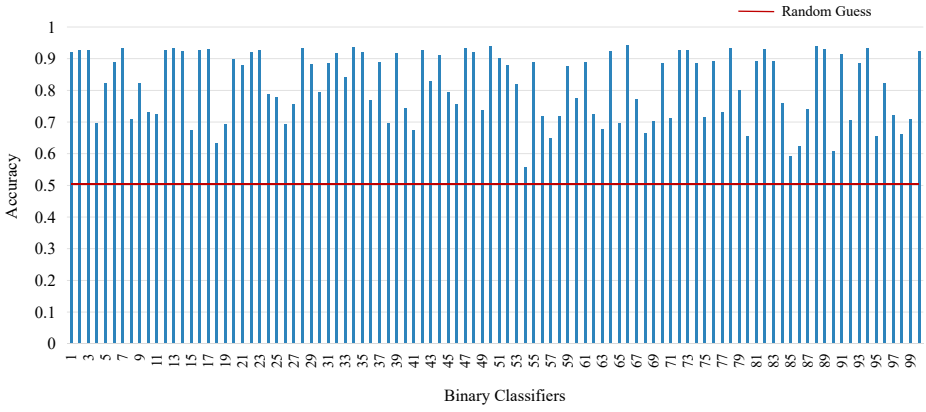

Figure 21: Classification accuracy across 100 binary classifiers.

H ROBUSTNESS TO NOISE

This section provides experiences on the robustness of our framework by inserting noise into the side channel traces. To this end, we evaluated the following three settings:

- **Gaussian noise insertion**: For each side channel data point $input$ on the side channel trace, $input = x \times n + (1 - x) \times input$, where $x \in [0.1, 0.2, 0.5]$, and n denotes randomly generated noise following the Gaussian Distribution.
- **Zero replacement**: Randomly set $x\%$ of the data points on the side channel trace to 0, where $x \in [10, 20, 50]$.
- **Round shifting**: Round shifting the side channel trace for x steps, where $x \in [1, 10, 100]$.

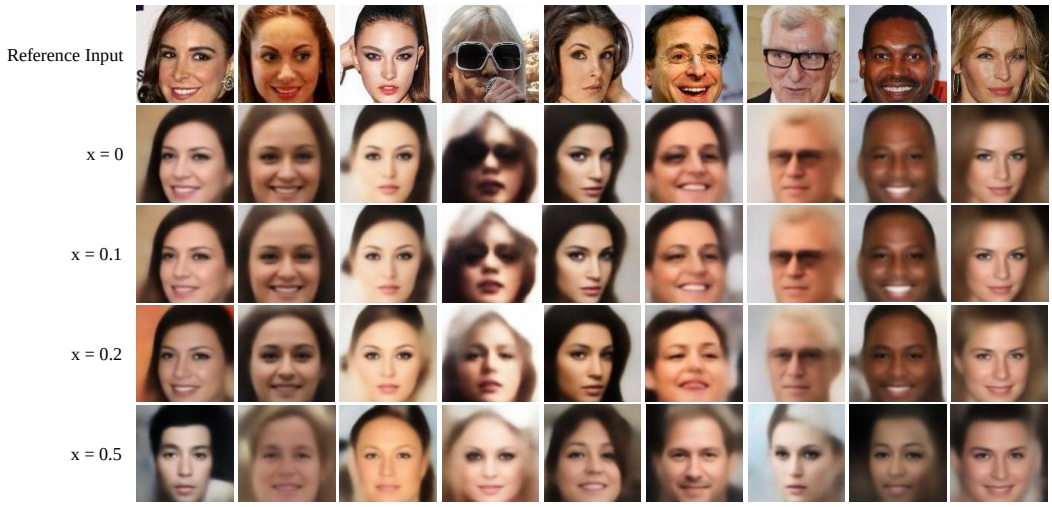

Figure 22: Evaluation results of `CelebA` dataset in terms of cache side channels and three different noise setting. We also present the synthesized images with no noise for the reference. User input images are presented on the first row for the reference.

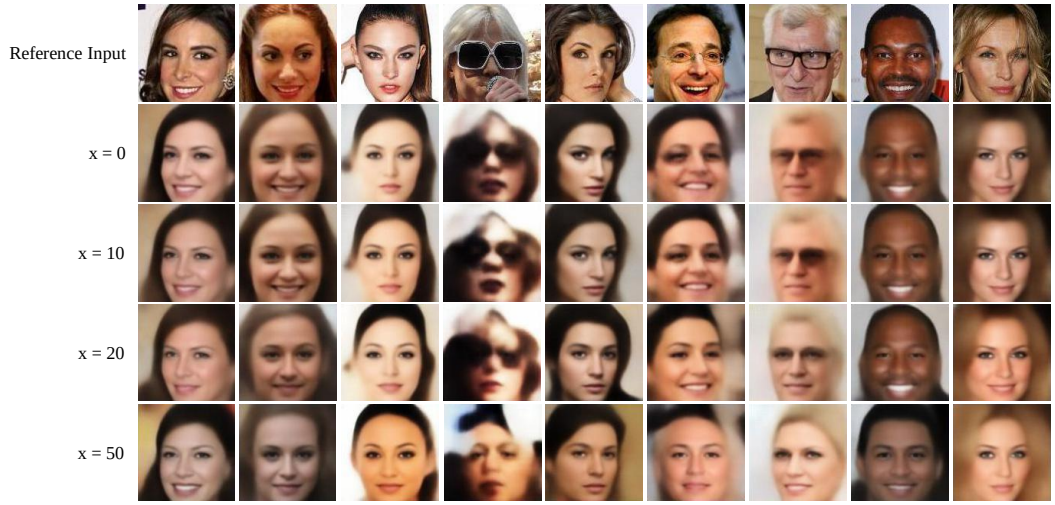

Figure 23: Evaluation results of `CelebA` dataset in terms of cache side channels and three different random zero replacement setting. We also present the synthesized images with no zero replacement ($x = 0$) for the reference. User input images are presented on the first row for the reference.

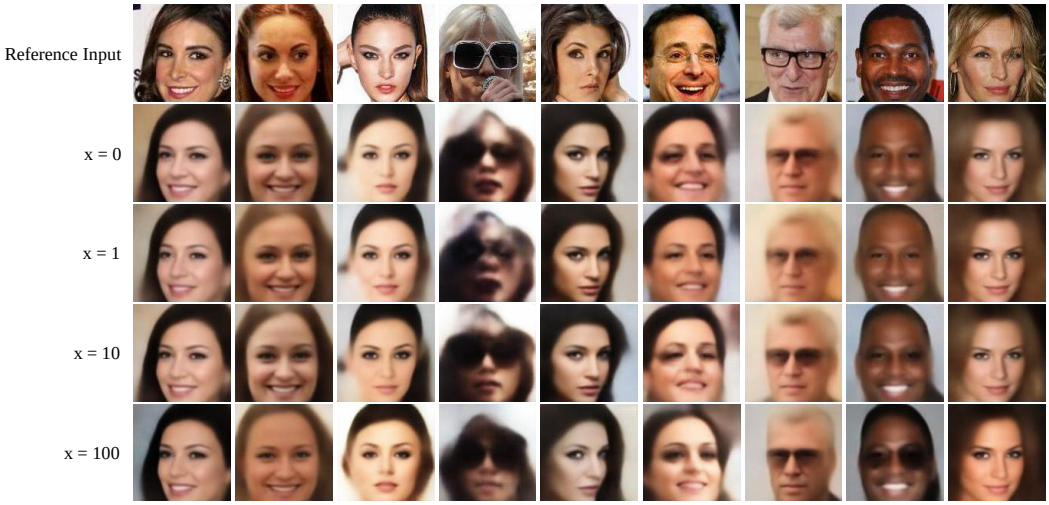

Figure 24: Evaluation results of `CelebA` dataset in terms of cache side channels and three different shifting setting. We also present the synthesized images with no shifting ($x = 0$) for the reference. User input images are presented on the first row for the reference.

We present the corresponding evaluation results in Fig. 22, Fig. 23, and Fig. 24, respectively. Overall, despite the challenging settings, we still observed considerable visually consistent features (e.g., face orientation, hair style, gender) between the reconstructed images and their reference inputs. Fig. 24 shows that round shifting seems to impose relatively low impact on the reconstructed images (e.g., comparing $x = 0$ with $x = 100$). In contrast, a more challenging setting, adding Gaussian noise to each side channel data point, causes observable effect on the constructed images (e.g., comparing $x = 0$ with $x = 0.5$).

I ABLATION EXPERIMENTS

This section provides more ablation experiments. We aim to demonstrate the necessity of *image encoder* and *a learned prior*. To this end, we launch experiences to synthesize images without using the image encoder (see the 4th row of Fig. 25), and also synthesize images with a fixed Gaussian prior (the 3rd row of Fig. 25). It is easy to see that the reconstructed images manifest much lower quality compared with images synthesized by our framework (the 2nd row of Fig. 25). In particular, images synthesized without using the image encoder are seen to contain grids (the last row of Fig. 25). Overall, we interpret these ablation evaluations highlight the importance of the image encoder and a learned prior in SCA.

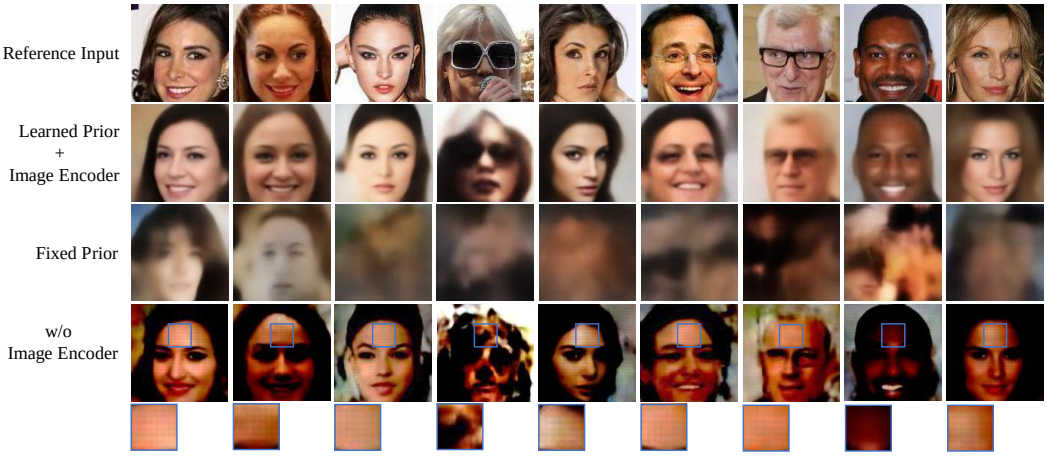

Figure 25: Evaluation results of `CelebA` dataset in terms of cache side channels and different settings. User input images are presented on the first row for the reference. Images synthesized by our presented framework are presented on the second row.